Int. J. Electrochem. Sci., 8 **(2013)** 2388 - 2406

International Journal of
ELECTROCHEMICAL
SCIENCE
www.electrochemsci.org

Platinum Activated IrO_2/SnO_2 Nanocatalysts and Their Electrode Structures for High Performance Proton Exchange Membrane Water Electrolysis

Junyuan Xu[1,2,3], *Qingfeng Li*[3], *Erik Christensen*[3,*], *Xindong Wang*[1,2] *and Niels J. Bjerrum*[3]

[1] State Key Laboratory of Advanced Metallurgy, University of Science and Technology Beijing, 30 College Road, Beijing 100083, China
[2] Department of Physical Chemistry, University of Science and Technology Beijing,
30 College Road, Beijing 100083, China
[3] Section of Proton Conductors, Department of Energy Conversion and Storage, Technical University of Denmark, Kemitorvet 207, DK-2800 Kgs. Lyngby, Denmark
[*]E-mail: erchr@dtu.dk

Received: 11 October 2012 / *Accepted:* 15 November 2012 / *Published:* 1 February 2013

In order to improve proton exchange membrane water electrolysis performance, anode catalyst and catalyst layer were examined in this work. SnO_2 supported IrO_2 nanocatalyst and its analogue with platinum enhancement were firstly synthesized for the oxygen evolution reaction. The effect of the introduction of Pt on the properties of the composites was explored by X-ray diffraction (XRD) and electrochemical test. Interaction between the introduced Pt nanoparticles and the bulk IrO_2/SnO_2 was evidenced in XRD. Electrochemical characterization showed the enhanced activitiy for the Pt activated IrO_2/SnO_2, which was attributed to the cooperative effects of improved electric conductivity and synergistic effect of Pt and IrO_2/SnO_2. Furthermore, catalyst layers based on IrO_2/SnO_2 catalysts were optimized with respect to microstructures, pore volume and pore size distribution. The performance was obviously improved due to the appropriate porosity and pore size distribution. The highest electrolyser performance of 1.63 V at 2 A cm^{-2} was achieved at 80 °C for optimized catalyst layers containing platinum activated IrO_2/SnO_2 catalyst.

Keywords: Proton exchange membrane water electrolysis; Catalyst layer; Platinum; Iridium-tin oxide; Pore structure

1. INTRODUCTION

As a potential energy carrier in the future systems based on renewable power sources, [1, 2] hydrogen is electrochemically reversible and therefore efficient in conversion via electrochemical devices, i.e. fuel cells and electrolysers. The biggest barrier to a hydrogen economy is the challenge of producing hydrogen economically to the point of use due to the technological issues of hydrogen storage and transportation. Today hydrogen is primarily produced by reforming of fossil fuels, e.g. natural gas, in a centralized way and distributed to the locations of use as a compressed gas. In long-term visions, however, decentralized production of hydrogen by means of water electrolysers is favorable in several ways. It is well known that when the usage rate is low, the electrolyser is a cheaper and simpler way for hydrogen production. When renewable energy sources e.g. hydropower, windmills or solar cells are considered, electrolysis is a practical way of converting the surplus electrical energy into chemical energy to be used whenever the power is required. A future can be envisioned, where a large number of photovoltaic panels and wind-driven generators are connected to electrolysers, and the hydrogen produced will be the major way of energy storage. In fact all long-term visions about the use of hydrogen as an energy carrier include water electrolysis as the central link of the technological chains.

Proton exchange membrane (PEM) water electrolysis has certain advantages such as higher current densities and purity of the product gases when compared with traditional alkaline liquid water electrolysis. Thus, it has gathered much research attention in recent years [3-5]. With respect to the efficiency, the majority of the overpotential that causes the energy loss in electrolysers is related to the electrochemical process at the anode, where the oxygen evolution reaction (OER) takes place. Development of active anode catalysts and preparation of catalyst layers are research topics in the performance improvement and energy consumption decrease of PEM water electrolysis.

Extensive research on anode catalysts is aimed at improved catalytic performance and reduced catalyst loading and cost. One method of achieving this in PEM fuel cells, is to disperse the electrocatalytic nanoparticles on high surface area support materials e.g. carbon blacks. However, carbon can be electrochemically oxidized at high potentials and cannot be used as catalyst supports for PEM water electrolysis. Many alternatives to carbon blacks as supports have been investigated for PEM water electrolysis, including Ti_nO_{2n-1} [6], SiC-Si [7], TiC [8], SnO_2 [9] and its commercial antimony doped form [10, 11]. In addition, some metal oxides such as SnO_2 [12], MoO_2 [13], Ta_2O_5 [14], MnO_2 [15] and TiO_2 [16] were also explored as dopants to form Ir- or Ru-based composite oxide catalysts. Further enhancement of the catalytic activity for (iridium) oxide catalysts was reported by introduction of a small amount of noble metals Pt [17-21]. Enhanced electrocatalytic performance was obtained due to specific interactions between Pt and the metal oxides and the continuous conduction path of electrons along Pt [17-21]. The first part of the present work was devoted to synthesis and further evaluation of a series of iridium based oxide catalysts supported on tin oxide nanoparticles as well as their analogues with the activating noble metal.

A catalyst layer is a core component, which determines the performance of fuel cells and water electrolysis. Concerning the fabricating techniques of catalyst layers, limited information is available from literature [22-26]. In general, the catalyst layer fabrication for PEM water electrolysis is very similar to that of PEM fuel cells. The performance of catalyst layers depends on technical parameters such as the catalytic activity of catalysts, the nature and content of the polymeric binder (sometimes it is an ionomer e.g. Nafion but PTFE is proposed to be used in combination with Nafion [24]) in the catalyst layers, the porous microstructure or the porosity and pore size distribution. For fuel cells, much work has been done to increase the electrochemical catalytic activity and decrease the mass transfer resistance by means of e.g. the preparation of multiple catalyst layers [27, 28], addition of PTFE [29-31], pore forming agents [32, 33] and other techniques [34-36].

Effects of the porosity and pore size distribution on the performance of the PEMFC and DMFC have been extensively investigated [33, 34, 37, 38]. You et al. [33] added magnesium sulfate to the fuel cell cathode catalyst layer as a pore forming agent to improve the DMFC performance. Addition of magnesium sulfate increased the pore number and volume and therefore improved access of reactants to the active sites of the catalyst layer. Sun et al. [34] attempted to spray catalysts directly onto the membrane at elevated temperatures in order to avoid the swelling or wrinkling of the Nafion membrane and found that the spraying and membrane surface temperatures influenced the PEMFC performance. Yim et al. [37] fabricated cathode catalyst layers with tailored microstructures by varying the hot-pressing pressure in a decal process. They found that water condensed and accumulated preferentially in the cathode catalyst layers with smaller pores due to the capillary equilibrium, which resulted in a serious decrease in the cell performance whereas the cathode catalyst layers containing larger pores exhibited much less diffusion problems and therefore better cell performance particularly in high-current density regions. Xie et al. [38] reported that the catalyst layer porosity and pore size distribution were altered with the type of catalysts, the preparation method and the Nafion content. A higher pore volume in the catalyst layers was preferred to possess more reaction sites and higher performance. In the second part of the present work, efforts were made to optimize the catalyst layer fabrication by using two types of selected catalysts. Finally water electrolysis cells were assembled and tested for evaluation of the prepared catalyst layers.

The aim of this study is to develop high performance PEM water electrolysis. For this purpose, platinum activated IrO_2/SnO_2 nanocatalysts and their electrode structures were developed in this work. Water electrolysis test was conducted at 80 $^{\circ}$C, showing a cell performance of 1.63 V at 2 A cm^{-2}.

2. EXPERIMENTAL

2.1. Preparation and evaluation of catalysts

2.1.1. Preparation of catalysts

The support (SnO_2) was synthesized by a sol-gel method, as described previously [9]. Briefly speaking, $SnCl_4$ (Analytical, Beijing Chemical Co, same for other chemicals unless otherwise specified) and citric acid were first dissolved in distilled water. Ammonia water (10 wt%) was then added to the solution to obtain a precipitate of $Sn(OH)_4$. Subsequently, the precipitate was heated to 70 $^{\circ}$C, and the pH was adjusted to 2 by addition of oxalic acid (30 wt%). The resulting hydrosol was mixed with polyethyleneglycol, which acted as a capping agent. The hydrosol was then filtered, washed with distilled water until the chloride residues completely disappeared, and dried at 80 $^{\circ}$C in a vacuum oven for 12 h. The resulting powders were finally heated up to 500 $^{\circ}$C for 2 h to obtain SnO_2.

For preparation of IrO_2/SnO_2, (in mass ratio of 2:1) catalysts, the precursors of $H_2Ir_2Cl_6 \cdot 6H_2O$ (supplied by Beijing Nonferrous Metal Research Institute) and $NaNO_3$ were first dissolved in distilled water and mixed with SnO_2 [9]. The water was gradually evaporated by heating the solution to 80 °C. The resulting salt mixture was placed in a muffle furnace and heated at 500 °C for 30 min. The fused salt-oxide mixture was then cooled down to room temperature and washed with distilled water to remove the remaining salts. The IrO_2/SnO_2 oxides were finally obtained by drying the mixture at 80 °C in a vacuum oven for 12 h.

The Pt activated IrO_2/SnO_2 (in mass ratio of 1:2:1) electrocatalyst particles were prepared by chemical reduction of H_2PtCl_6 (supplied by Beijing Nonferrous Metal Research Institute) on the obtained IrO_2/SnO_2 oxide powders using formic acid as a reducing agent. In the process, IrO_2/SnO_2 was first suspended in a mixture of distilled water and glycerol (in volume ratio of 1:1), and sonicated for 60 min before the H_2PtCl_6 solution was added under stirring. The pH of the mixture was adjusted to 9 by dropwise addition of 0.5 mol L^{-1} NaOH solution. The mixture was held at room temperature for 10 h under magnetic stirring and nitrogen bubbling. Subsequently, a formic acid solution (10 wt%) was added to the mixture at 80 °C under stirring for 30 min. The mixture was then cooled to room temperature, centrifuged and rinsed for several times with distilled water. The obtained catalyst powders were finally dried in a vacuum oven. In parallel Pt black was prepared as a reference.

2.1.2. Characterization of catalysts

XRD analysis of the catalysts was performed with a Marcogroup diffractometer (MXP21 VAHF) with a Cu-Kα radiation source (λ = 0.154056 nm) to characterize the catalyst's crystalline structure.

Electrochemical properties of the catalysts were characterized by cyclic voltammetry (CV), electrochemical impendence spectroscopy (EIS) and polarization curve in a 0.1 mol L^{-1} H_2SO_4 solution at 25 °C using a VMP2 electrochemical workstation (Princeton, USA). The catalyst layer was deposited on a tin oxide-coated titanium plate (20mm * 10mm * 1 mm) with an effective area of 1cm^2 by the following method: a mixture containing 2 mL of isopropyl alcohol, 10 mg of catalyst, 33 mg of Nafion solution (5 wt%, Dupont) and 27 mg of the PTFE emulsion (6 wt%, Shanghai Organic Fluorine Material Research Institute) was mixed for 30 min in an ultrasonic bath. An aliquot of the mixture (200 μL) was placed on the substrate surface and dried at 70 °C. The catalyst layer was submersed in a sodium chloride solution for 2 h to convert the H^+ form of the Nafion ionomer to a salt form and then heat-treated at 340 °C for 30 min for the PTFE sintering. After cooling to room temperature, the catalyst layer was finally immersed in water to restore the H^+ form of the ionomer, meanwhile, silver nitrate solution was used to detect Cl^-.

All measurements were carried out in a three-electrode cell. A platinum foil and saturated calomel electrode (SCE vs. SHE 0.24 V) were used as the counter electrode and reference electrode, respectively. The electrolyte was deoxygenated via bubbling with N_2 prior to and during all measurements. The scan range of the CV was 0 to 1 vs. SCE/V, and the scan rate ranged from 2 to 300 mV s^{-1}. The EIS measurements were conducted at 1.18 vs. SCE/V in the range of 5 mHz to 99 kHz, and a 10 mV amplitude of the sinusoidal potential perturbation was used. The impedance data were modeled with ZSimpWin software. The scan range of the polarization curve was 1 to 1.8 vs. SCE/V, and the scan rate was 1 mV s^{-1}. Each point was obtained by setting the potential anodically in a 1 mV step with a holding time of 1 s, which was found to be enough for reaching a stabilized current density.

2.2. Preparation and optimization of catalyst layers

2.2.1. Preparation and physical analysis of catalyst layers

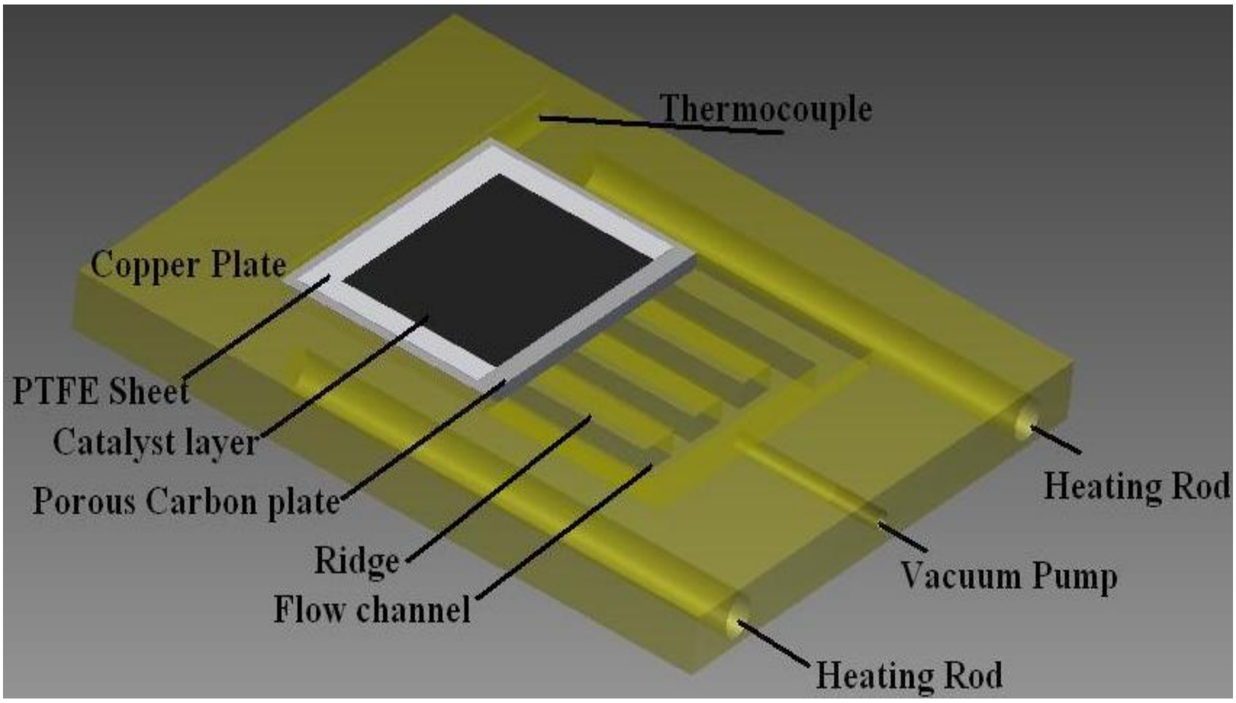

Figure 1. The device used for the preparation of catalyst layers.

The preparation of catalyst layers was schematically shown in Fig. 1. In the preparation process of catalyst layers, a PTFE sheet was first placed on top of a porous carbon plate, which was fixed on a copper plate. During the deposition of the catalysts, the PTFE sheet remained fixed on the plate with the help of a vacuum pump. The substrate was heated using two heating rods, and the temperature was measured by a thermocouple. The anode catalyst layer was fabricated by direct spray deposition of 4.5 mL ink (containing anode catalyst, 5 wt% Nafion solution, 6 wt% PTFE emulsion, and isopropyl alcohol as solvent) onto the PTFE sheet at varied parameters, as listed in Table 1. The weight ratio of anode catalyst, Nafion and PTFE was fixed at 14:2:1. The spray velocity was 0.1 mL min^{-1}, and thus the spray time at each spraying process was about 45 minutes. Eventually, a spraying process was attempted by setting the substrate temperature in steps during the spraying, i.e. at 85 °C for 15 minutes, 65 °C for 15 minutes and finally 38 °C for another 15 minutes. After being immersed in the sodium chloride solution for 2 h and heat-treated at 340 °C for 30 min, the anode catalyst layers were immersed in water for 2 h. For all anode catalyst layers, the loadings of Nafion and PTFE were at 0.2 and 0.1 mg cm^{-2}, respectively.

Table 1. Anode catalyst layers prepared with varying parameters.

Anode Catalysts	Substrate Temperature (˚C)	Spraying Time (min)	$E_{2Acm^{-2}}$ (V)
IrO_2/SnO_2(1.2 mg cm^{-2} IrO_2)	38	45	1.72
IrO_2/SnO_2(1.2 mg cm^{-2} IrO_2)	65	45	1.69
IrO_2/SnO_2(1.2 mg cm^{-2} IrO_2)	85	45	1.80
IrO_2/SnO_2(1.2 mg cm^{-2} IrO_2)	86→65→39	15→15→15	1.66
Pt-IrO_2/SnO_2(0.3 mg cm^{-2} Pt, 0.6 mg cm^{-2} IrO_2)	85→65→37	15→15→15	1.63

An ink composed of 40 wt% Pt/C (Johnson Matthey) catalyst, Nafion solution and isopropyl alcohol was sprayed on a PTFE sheet to form the cathode catalyst layers. The loading of 40 wt% Pt/C and Nafion was 0.5 and 0.1 mg cm^{-2}, respectively.

The morphology of anode catalyst layer surfaces was investigated by the scanning electron microscope (SEM, Zeiss SuprATM 55 microscope). The pore size distribution of the anode catalyst layer was determined by N_2 gas adsorption/desorption measurement (Autopore IV 9500, Micromeritics).

2.2.2. Single cell assembly and evaluation

The pretreatment of Nafion 212 membranes (Dupont) was accomplished by successive treatment in 5 wt% H_2O_2 solution, distilled water, 8 wt% H_2SO_4 solution and then in distilled water again, at 80 ˚C for 60 min each step. The catalyst coated membranes (with a 1.5 cm^2 active area) was obtained by transferring the catalyst layers from the PTFE sheets to the pre-treated Nafion 212 membrane by the decal method under the conditions of 135 ˚C and a pressure of 75 kg cm^{-2} for 3 min.

The water electrolysis performance was tested by using a single cell. The end plate was made of stainless steel while two gold coated titanium plates with gas flow channels were used as current collectors and Teflon sheets as gaskets. Carbon cloth was used as porous GDL layers for both anode and cathode. The water electrolysis was operated at 80 ˚C and under the ambient pressure. Distilled water was fed to the anode and cathode at a flow rate of 3 mL min^{-1}. The impedance measurement was carried out at 1.54 V and the frequency varied from 5 mHz to 99 kHz by a VMP2 electrochemical workstation. The cathode of the cell was used as both the counter and reference electrode. Polarization curves were measured in constant current mode by increasing the current density from 0 to 2 A cm^{-2}.

3. RESULTS AND DISCUSSION

3.1. Characterization of Pt-IrO_2/SnO_2 catalysts

3.1.1. XRD

The crystal structures of the prepared IrO_2/SnO_2, Pt-IrO_2/SnO_2 and Pt black catalysts were examined by XRD, as shown in Fig. 2. As seen from the figure, for IrO_2/SnO_2, all peaks matched a rutile structure. The unsupported Pt black was produced under the same condition as for the deposited Pt-IrO_2/SnO_2. Diffraction peaks of {111}, {200}, {220}, and {311} plane were observed for Pt black catalysts at 2θ values of 39.90, 46.62, 67.68, 81.49^o showing the typical character of a crystalline Pt face-centered cubic (fcc) phase.

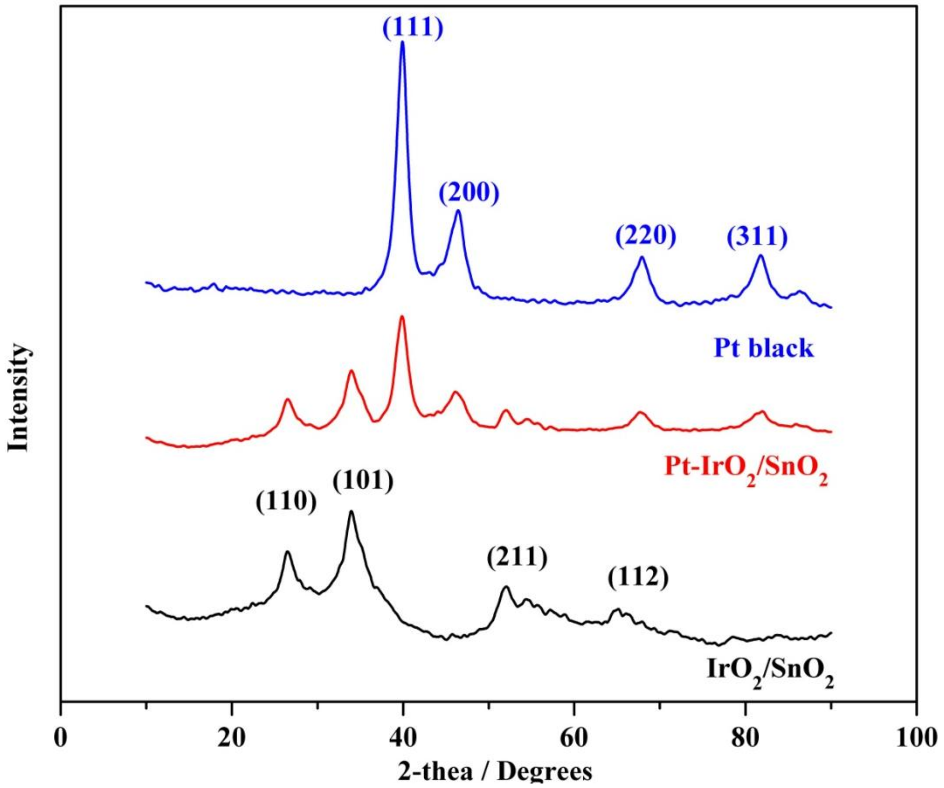

Figure 2. XRD patterns of IrO_2/SnO_2, Pt black and Pt activated IrO_2/SnO_2 Powders.

Compared with the unsupported Pt black, however, the XRD responses of the Pt deposited on IrO_2/SnO_2 supports slightly shifted to higher angles, i.e. at 40.02, 46.64, 67.85, 81.59^o, respectively, which was also observed in the previous report [19, 20]. This indicated a lattice contraction and therefore some interaction between Pt and the IrO_2/SnO_2 supports.

3.1.2. Electrochemical analysis

The electrochemical performances of the two oxygen evolution electrocatalysts were evaluated by the CV, EIS and polarization curve measurements. The obtained voltammograms, though not shown, exhibited typical broad waves featuring the oxide electrodes in dilute sulfuric acid electrolytes. Electrochemically the capacitance of the oxide electrodes results from two contributions, the pseudo-capacitance due to the charge storage by the solid-state redox reactions of Ir or Pt on the surface of the catalysts and the standard double layer capacitance due to the charging/discharging of the electrode - electrolyte interface [10, 16, 39]. An approach to the voltammetric charge (Q^*) measurement by means of integration of the anodic sweep of the voltammogram was suggested by Ardizzone et al. [40] for characterization of electrochemically active surface area of noble metal oxide electrodes. They assumed that for such electrodes, there are two types of the catalytic surface areas, an “outer” surface which is easily accessible for the redox reactions and an “inner” surface where the redox reactions are hindered by the difficulty of access of reactant species e.g. proton donating species.

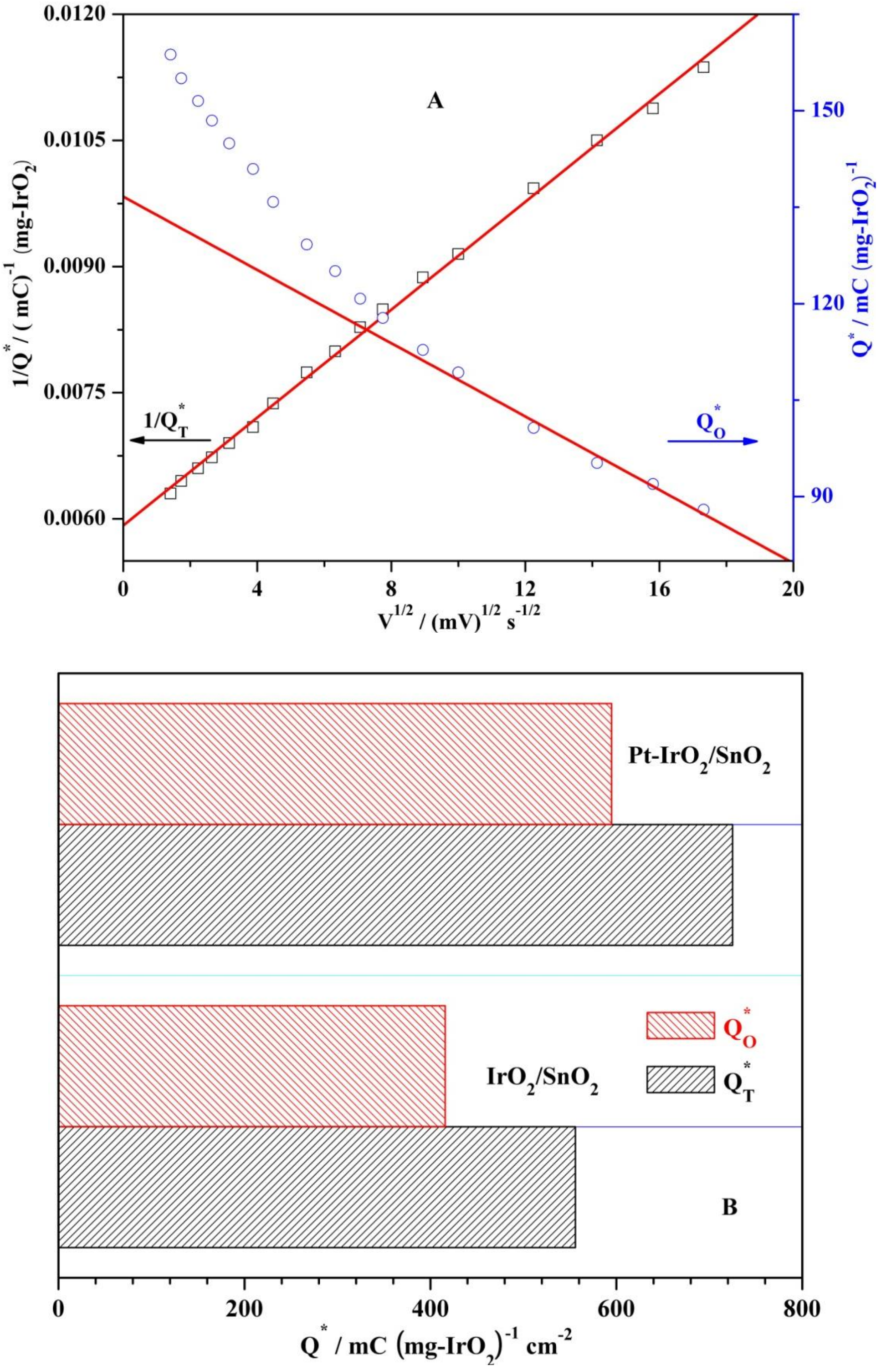

Figure 3. (A) Illustration of obtaining the voltammetric total (Q_T) and outer (Q_O) charges from voltammograms at varied scan rates. (B) Results of the total and outer charges for two oxygen evolution catalysts. The physical meanings of the total and outer charges are explained in the text.

Two parameters are therefore proposed as the "outer" voltammetric charge (Q_O^*) and the total voltammetric charge (Q_T^*), corresponding to the easily accessible active surface area and the overall surface area of the catalyst layer, respectively. According to Ardizzone et al. [40], the voltammetric charge (Q^*) is a function of the scan rate (ν) following equation (1) at high scan rates and equation (2) at lower scan rates.

$$Q^*(\nu) = Q_O^* + A \cdot \frac{1}{\sqrt{\nu}} \qquad (1)$$

$$\frac{1}{Q^*(\nu)} = \frac{1}{Q_T^*} + B \cdot \sqrt{\nu} \qquad (2)$$

The correlations are schematically illustrated in Figure. 3A. The outer voltammetric charge (Q_O^*) can be obtained by extrapolation of the Q^* versus $\frac{1}{\sqrt{\nu}}$ curve to the charge at an infinite scan rate while the total voltammetric charge (Q_T^*) can be obtained by extrapolation of the $\frac{1}{Q^*(\nu)}$ versus $\sqrt{\nu}$ curve to the zero scan rate. The results of the outer and total voltammetric charges, corresponding to the easily accessible and overall surface area of the two types of OER electrocatalysts, are summarized in Figure. 3B. As shown in the figure, For the Pt-IrO_2/SnO_2 catalyst, both the outer and total voltammetric charges or the easily accessible and overall surface area for the Pt-IrO_2/SnO_2 were even higher than those for the IrO_2/SnO_2.

The electrocatalysts were characterized by EIS, as shown in Fig. 4A. The measurements were made at 1.18/V vs SCE, which was within the typical oxygen evolution potential range. A set of EIS parameters for the two types of catalysts were obtained by fitting the experimental data using the ZSimpWin software and were summarized in Table 2.

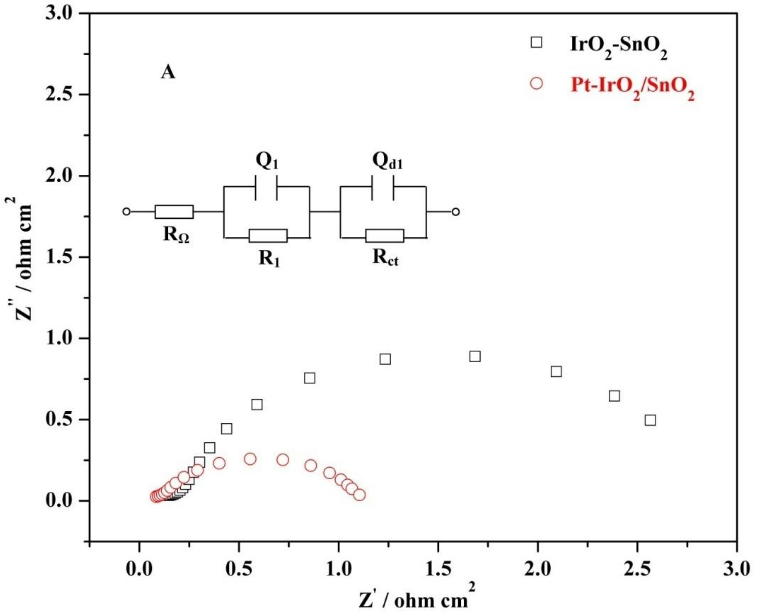

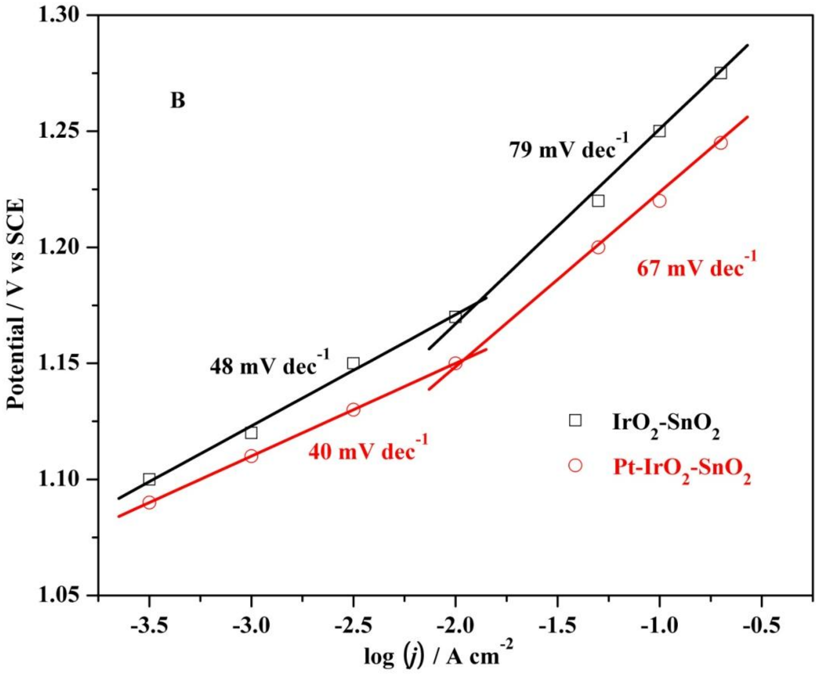

Figure 4. (A) Nyquist diagrams of two oxygen evolution catalysts measured in 0.1 mol L^{-1} H_2SO_4 at 1.18 vs. SCE/V and 25 °C. (B) Tafel plots of three oxygen evolution catalysts in 0.1 mol L^{-1} H_2SO_4 at 25 °C.

The equivalent circuit that was most closely matching the observed impendence diagrams is depicted by R_Ω (R_1Q_1) ($R_{ct}Q_{d1}$) in the figure. R_Ω was the ohmic resistance of working electrode and electrolyte between working electrode and reference electrode. R_{ct} was the charge-transfer resistance of a faradic process occurring at the oxide/electrolyte interface. The capacitive elements were represented by Q, which was a constant phase element (CPE) often used to model the depressed semi-circles due to heterogeneities and surface roughness. Here, Q_{d1} included both the double-layer capacitance of the oxide-electrolyte interface and the pseudocapacitance of catalysts. This type of model has generally been used to interpret the impendence data of IrO_2 or RuO_2 where the R_1Q_1 circuit was assumed to be attributable to different phenomena, e.g, ionic or electronic transport phenomena [41], effect promoted by the presence of pores in the electrode coating [42] or the resistive effect of the Ti_2O_3/TiO_2 interlayer on the titanium substrate [43].

As seen from Table 2, the overall ohmic resistance (R_Ω) of IrO_2/SnO_2 electrocatalysts was approximately 0.15 ohm cm^2, which is nearly twice as high as that of the Pt activated IrO_2/SnO_2 electrocatalysts (0.08 ohm cm^2). The conductivities of IrO_2/SnO_2 and Pt-IrO_2/SnO_2 were also tested using the similar method reported previously [44] and 0.09 and 12 S cm^{-1}, respectively. The charge-transfer resistance (R_{ct}) in the low frequency range, a measure of the polarization resistance or the catalytic inactivity of the electrode, is directly related to the OER kinetics. As seen from the Table, the R_{ct} was considerably decreased from 2.49 Ω cm^2 for IrO_2/SnO_2 and to 1.02 Ω cm^2 for Pt-IrO_2/SnO_2 catalysts, showing the steady enhancement of the catalytic activity for the three catalysts in the order.

Table 2. Impedance parameters obtained from fitting the experimental data to the R_{Ω} (R_1Q_1) $(R_{ct}Q_{d1})$ circuit, as shown in Figure 4A.

	R_{Ω} (Ω cm^2)	Q_{d1} (mF cm^{-2})	R_{ct} (Ω cm^2)
IrO_2 [9]	0.15	234	3.59
IrO_2/SnO_2 [9]	0.15	330	2.49
Pt- IrO_2/SnO_2	0.08	420	1.02

Moreover, the overall capacitance (Q_{d1}), a measure of the active surface of the catalysts [45], was found to be 330 and 420 mF cm^{-2} for the two catalysts. In brief, the low charge-transfer resistance and the high capacitance or active surface area for the Pt-IrO_2/SnO_2 electrocatalyst suggested the enhanced catalytic activity for oxygen evolution.

Tafel slopes for the ohmic resistance compensation polarization curves are shown in Fig. 4B. Two region polarization curves with different Tafel slopes were observed through the entire current density ranges. At low overpotential ranges, the slopes of IrO_2 or RuO_2 was about 30-60 mV dec^{-1}, whereas the slopes reached to 70-130 mV dec^{-1} when the overpotential was increased [46-48]. As shown in Fig. 4B, the measured value corresponded to previously reported results [46-48], and in the entire current density ranges, the Tafel slopes of Pt-IrO_2/SnO_2 electrocatalyst was lower than those of IrO_2/SnO_2 electrocatalyst, indicating the better activity for oxygen evolution. In fact the activity of Pt towards oxygen evolution is lower than that of IrO_2. It is interesting that the addition of Pt did not decrease the reaction kinetics of IrO_2, but actually enhanced the catalytic activity considerably. The enhanced electrocatalytic performance is probably related to a higher conductivity of the composite and a possible specific interaction between Pt and IrO_2/SnO_2, as suggested on in previous report [17-21].

3.2. Optimization of catalyst layers using IrO_2/SnO_2

3.2.1. SEM of the sprayed catalyst layer surfaces

Fig. 5 showed the SEM images of the catalyst layer sprayed on PFTE sheets at different substrate temperatures using IrO_2/SnO_2 catalyst.

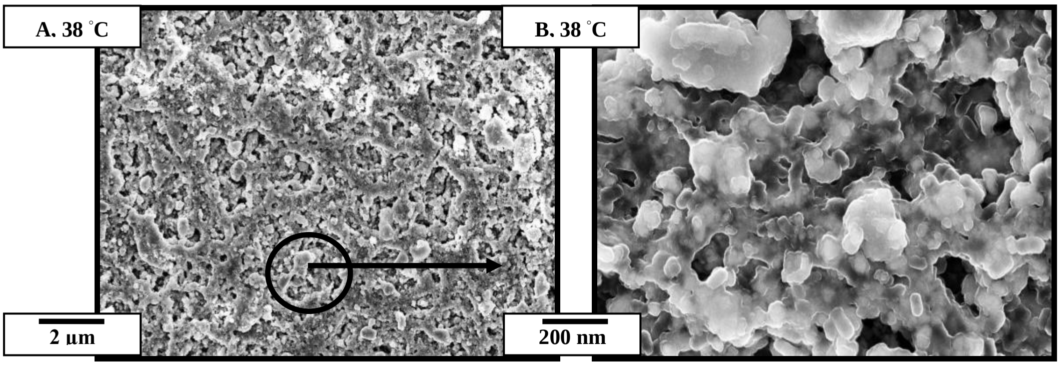

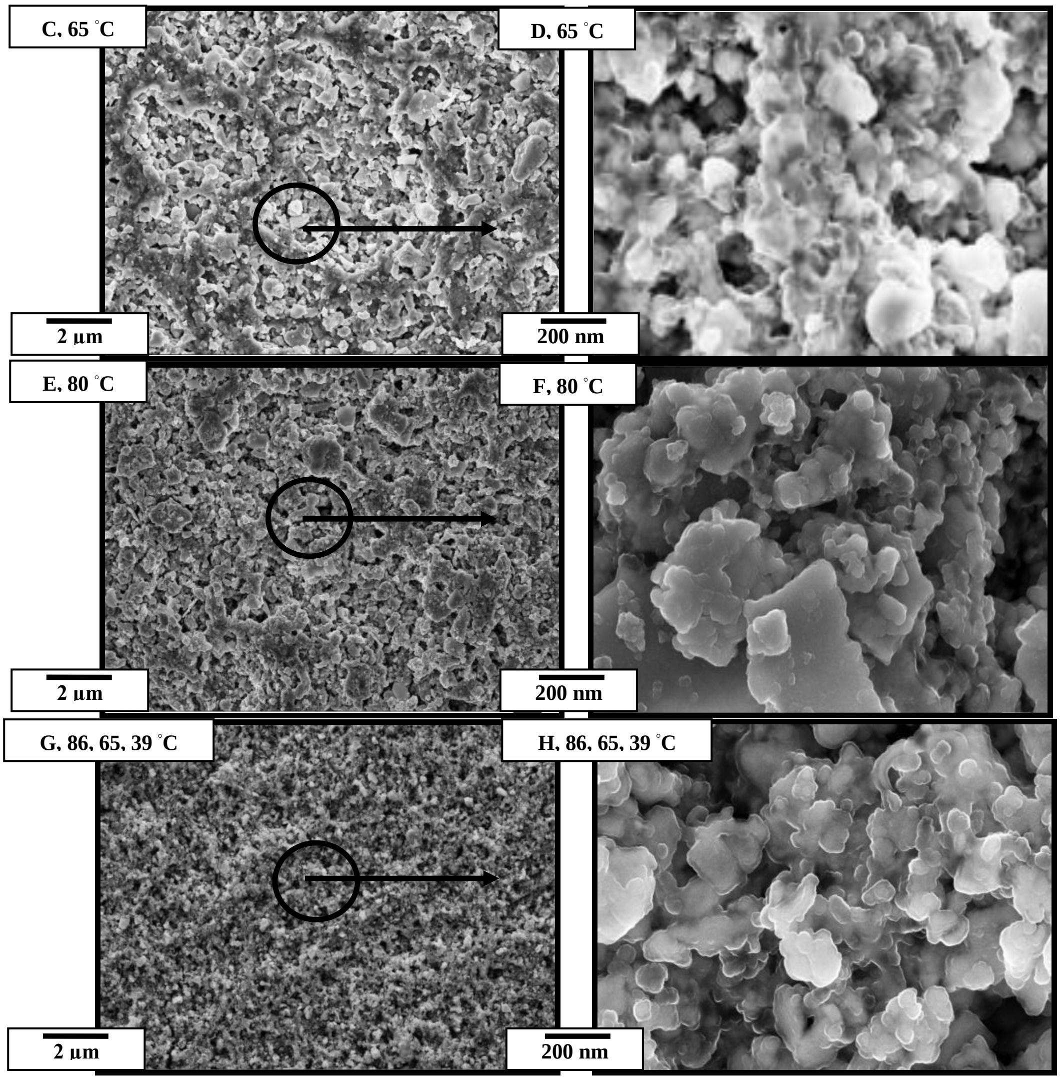

Figure 5. SEM images of the catalyst layers sprayed at different substrate temperatures as specified in the figure using the same batch of IrO_2/SnO_2 (in mass ratio of 2:1) catalysts. The magnification was 3K for A, C, E, G and 50K for B, D, F, H.

Fig. 5A and 5B were reproduced from the previous work [24]. As rationalized previously [24], the presence of a highly hydrophobic PTFE phase in the conventionally Nafion-bonded hydrophilic catalyst layer formed a hydrophilic-hydrophobic meshwork with well distributed pore structure allowing for liquid water access and gas product removal.

The influence of substrate temperature during spraying may be attributed to the evaporation rate of isopropyl alcohol (its boiling point is 82.5 °C). As shown in Table 1, since the gasification of isopropyl alcohol was endothermic in nature, to achieve a substrate temperature of 38, 65 and 85 °C during the spraying, the initial setting temperatures were 50, 80 and 100 °C, respectively. It suggested that a large amount of isopropyl alcohol in the ink might still be in the liquid state when it reached the PTFE sheet at temperatures below its boiling point temperature. When the ink was sprayed into the PTFE sheet surface, the catalyst layer was drying as the solvent evaporated and the catalyst particles started packing and forming mircrostructures.

By elevating the substrate temperature to 65 ˚C, evaporation of the solvent was faster and so was the catalyst particle packing (Fig. 5C and 5D), when compared with the catalyst layer surface sprayed at a substrate temperature of 38 ˚C (Fig. 5A and 5B). This was expected to increase the porosity as well as to alter the pore size distribution of the catalyst layer.

When the spraying substrate temperature was further increased to 85 ˚C, most of isopropyl alcohol would evaporate as soon as it reached the PTFE sheet. As a result, the catalyst particles gathered together and packed closely. The meshwork on the catalyst layer surface disappeared and large catalyst clusters were observed, as shown in Fig. 5E and 5F.

Finally, a spraying process was attempted in which the substrate temperature was set in steps during the spraying, i.e. at 85 ˚C for 15 minutes, 65 ˚C for 15 minutes and finally 38 ˚C for another 15 minutes. The obtained catalyst layer surface is shown in Fig. 5G and 5H. It suggested that the porosity and pore size reached values between what was found for the catalyst layers as sprayed at the substrate temperatures of 65 and of 85 ˚C, respectively.

3.2.2. BET of the sprayed catalyst layers

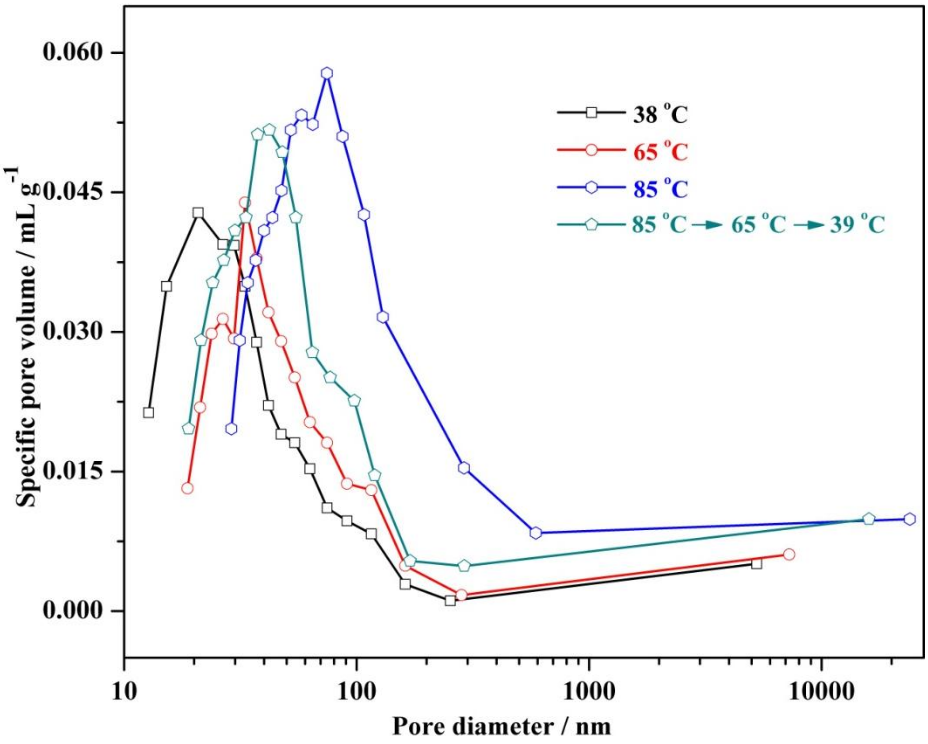

Figure 6. The specific pore volume and pore size distribution of the sprayed catalyst layers from the same batch of IrO_2/SnO_2 (in mass ratio of 2:1) catalyst but at varied substrate temperatures.

Fig. 6 shows the specific pore volume and pore size distribution for the four catalyst layer samples sprayed at varied substrate temperatures. For the catalyst layer as sprayed at the substrate temperature of 38 ˚C, the major pores in the catalyst layer were located in a pore size range from 10 to 100 nm, indicating that mesopores (2-50 nm) and macropores (>50 nm) were dominating in the catalyst layer. By increasing the substrate temperature from 38 to 65 and 85 °C, a clear shift in the pore size distribution curves was observed. The peak point of the curves shifted from 18 to 33 and further to 74 nm. The shift was accompanied with a significant increase in the specific pore volume or in the porosity of the catalyst layers. These findings are in good agreement with the SEM examinations discussed above. By doing the spraying with stepped temperature settings, a pore size distribution and specific pore volume was achieved in the range between those as sprayed at the substrate temperatures of 65 and 85 °C. In brief, by setting the substrate temperatures the porosity, pore size and distribution can be tailored to a noticeable extent, which is expected to influence and optionally optimize the electrode performance, as to be discussed below.

3.2.3. Water electrolysis performance of the sprayed catalyst layers

The performance of water electrolysis cells based on the catalyst layers sprayed at different substrate temperatures using IrO_2/SnO_2 catalysts was shown in Fig. 7.

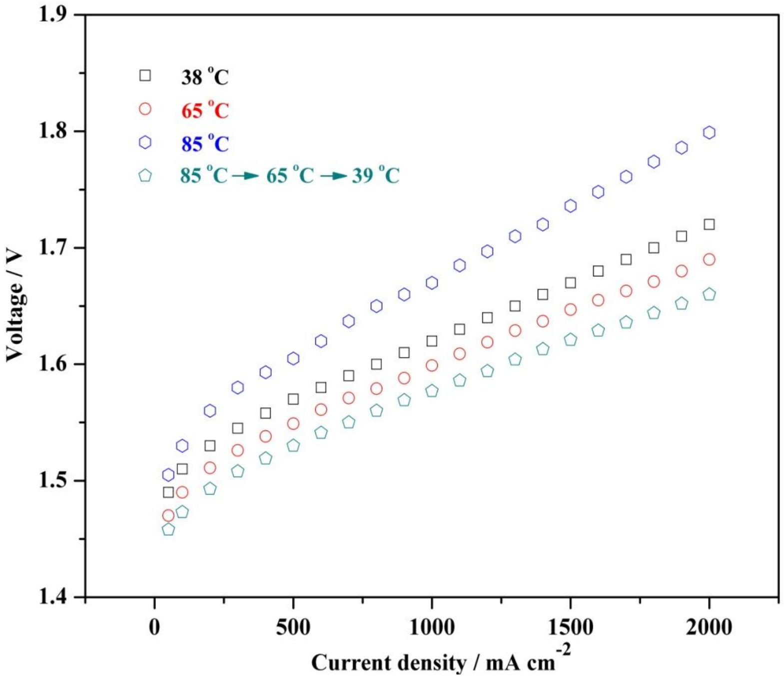

Figure 7. Polarization curves of water electrolysis cells using the catalyst layers sprayed at different substrate temperatures with the same IrO_2/SnO_2 catalyst (in mass ratio of 2:1). The electrolysis was operated at 80 °C and under ambient pressure. The membrane used was Nafion 212. The anodic loading of IrO_2 was 1.2 mg cm^{-2} and the cathode was made from 40 wt% Pt/C at a loading of 0.2 mg Pt cm^{-2}.

The cell voltage for the catalyst layer sprayed at substrate temperature of 38 °C was 1.72 V at 2 A cm^{-2} (expressed as $E_{2Acm^{-2}}$). By increasing the substrate temperature from 38 to 65 °C, an increase in the specific pore volume or in the porosity of the catalyst layers was observed from SEM in Fig. 5 and the pore size distribution in Fig. 6. As a result, better water electrolysis performance ($E_{2Acm^{-2}}$ = 1.69 V) was obtained in the whole current density region. However, after increasing the substrate temperature from 65 to 85 ˚C, the water electrolysis performance ($E_{2Acm^{-2}}$ = 1.80V) was poor, probably indicating that the large catalyst clusters and too high porosity degrade water electrolysis performance of the catalyst layers. As shown in Fig. 6, an intermediate range of the pore size distribution and specific pore volume was achieved by the step-setting of the substrate temperature. Thus obtained catalyst layers exhibited the best water electrolysis performance ($E_{2Acm^{-2}}$ = 1.66V).

3.2.4. EIS of the sprayed catalyst layers

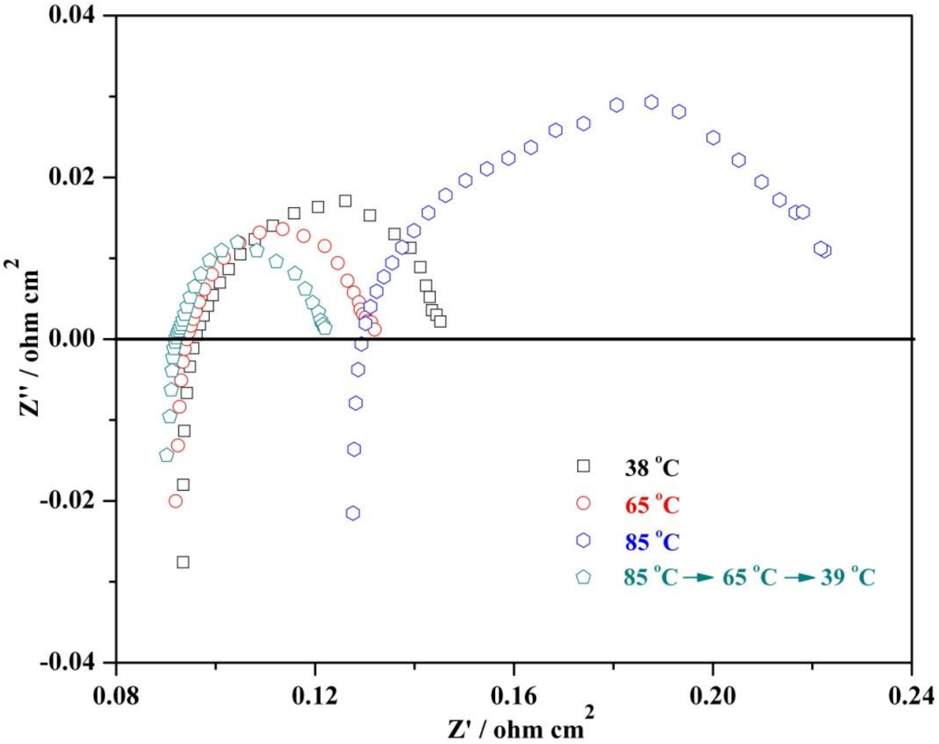

Figure 8. The EIS of sprayed catalyst layers from the same batch of IrO_2/SnO_2 (in mass ratio of 2:1) catalysts but at varied substrate temperatures. The EIS was measured at 1.54V and 80 ˚C.

As mentioned above, the improved performance could be mainly attributed to the optimized pore size distribution and porosity. In order to further prove this statement, the EIS was measured at 80 ˚C and 1.54 V for the catalyst layers from the same batch of IrO_2/SnO_2 catalysts but at varied substrate temperatures, as shown in Fig. 8. The EIS data of the catalyst layer sprayed at substrate temperature of 38 ˚C was reproduced from our previous work [24].

By increasing the substrate temperature from 38 to 65 ˚C, similar meshwork structures were obtained with no visible cracks, as observed by the SEM images, and with increased specific pore volume or porosity, as shown in Fig. 6. The former was essential for the electron and proton conductivity while the latter was critical for the liquid water access and oxygen removal. At a cell voltage of 1.54V or higher, the catalytic reaction rate was significant, not just depending on the catalytic activity but also on the mass transport processes, because the bubbling effect would imply when the oxygen evolution rate was high [24, 49]. In this situation, the real surface area of catalysts would be reduced as gas bubbles were stuck to the catalyst surface or clogged the pores. The increased porosity would therefore create open paths for the oxygen removal from the catalyst layer as well as for the supply of the water to the catalytic active sites. As a result, similar high frequency intercept (internal resistance) with the real axis but smaller arc (catalytic reaction rate) at low frequency were observed.

However, after increasing the substrate temperature from 65 to 85 °C during the catalyst layer preparation, the meshwork disappeared as catalysts formed clusters and the catalyst layer porosity improved. This was illustrated by the larger high frequency intercept and low frequency arc in the EIS. As expected, the catalyst layer sprayed with setting temperatures decreased in steps presented the smallest high frequency intercept and low frequency arc, corresponding to a better electrolyser performance.

3.4. Water electrolysis performance of using Pt activated catalysts

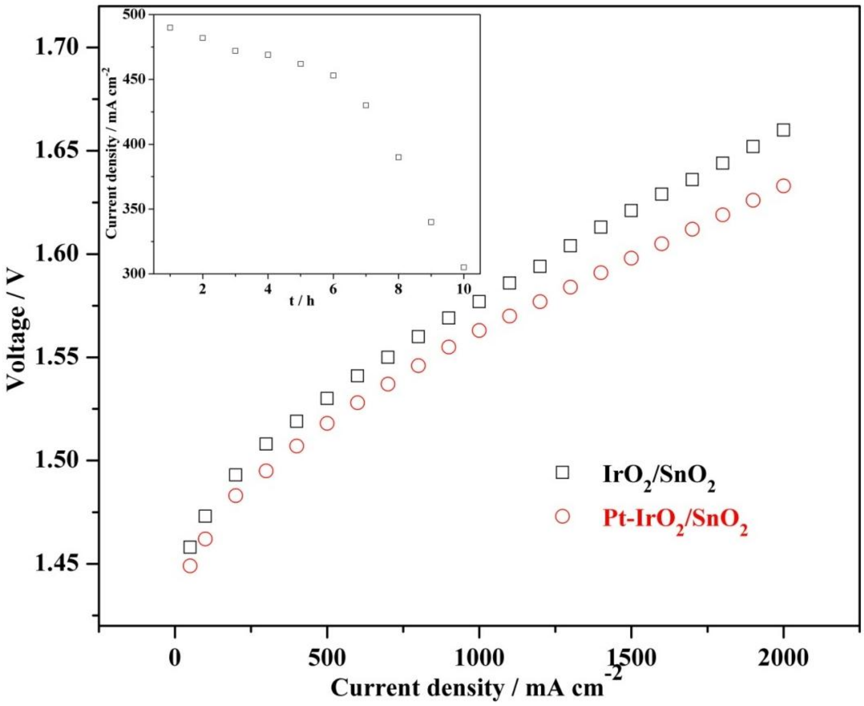

Figure 9. Polarization curves of water electrolysis cells based on IrO_2/SnO_2 (1.2 mg cm^{-2}, IrO_2) and Pt-IrO_2/SnO_2 (0.3 mg cm^{-2} Pt, 0.6 mg cm^{-2} IrO_2) catalysts operating at 80 °C and ambient pressure with Nafion 212 membrane. The anode catalyst layer was sprayed with step-setting temperatures. The cathode was made of 40 wt% Pt/C at a loading of 0.2 mg Pt cm^{-2}. The inset showed the short-term stability test of Pt-IrO_2/SnO_2 catalyst at 1.52 V and 80 °C.

After the optimization of the catalyst layer (sprayed with substrate setting temperatures being decreased in steps), the Pt-IrO_2/SnO_2 catalyst was then applied to fabricate the catalyst layer. Fig. 9

showed the corresponding PEM water electrolysis performance. As seen from the figure, in the low current density range, where the catalytic activity dominated the cell performance, improvement in the cell performance was observed for the Pt activated IrO_2/SnO_2 catalysts, as compared with that for the IrO_2/SnO_2 catalysts. No visible sign of mass transport hindrance was observed at current densities of up to 2 A cm^{-2}. At current densities higher than 200 mA cm^{-2}, the polarization of water electrolysis was apparently dominated by the ohmic loss and thus the improved cell performance for the Pt activated catalysts might be due to reduced ohmic resistance of the catalyst layer as well. It should be noted that the cell performances for Pt-IrO_2/SnO_2 in Fig. 9 were achieved at low noble metal loadings. A cell voltage of 1.63 V at a current density of 2 A cm^{-2} was achieved at a total noble metal (Ir and Pt) loading of 1.1 mg cm^{-2}, a performance similar to [26] or better [14, 50-52] than that of previous works.

This is indeed a very high performance, but it must be noted that there are some stability problems of the labscale single cell setup used here. The inset in Fig. 9 shows the short-term stability of Pt-IrO_2/SnO_2 catalyst at 1.52 V and 80 °C. The corrosion of the carbon cloth anodic gas diffusion layer apparently resulted in a weak contact between this layer and the catalyst layer, which decreased the performance with time. As seen from the inset, during the initial 5 hours, the performance decreased moderately, but after that the performance decreased rapidly. As a result, the performance shown in the paper was always recorded during the initial 2 hours. However, the setup was used here for comparison of activity of various catalysts in the labscale, and longtime stability of the diffusion layers was therefore considered of less importance.

4. CONCLUSIONS

SnO_2 supported IrO_2 nanocatalyst and its platinum-activated analogue were synthesized and characterized for the oxygen evolution reactions. Electrochemical characterization in 0.1 mol L^{-1} H_2SO_4 at room temperature showed the enhanced activities for the Pt-IrO_2/SnO_2, which were attributed to the cooperative effects of improved electric conductivity and the possibly synergistic effect of Pt and IrO_2/SnO_2. Using the catalysts, catalyst layers with tailored microstructures and optimized pore volume and pore size distribution were fabricated by a spraying process using of stepwise decreasing of substrate temperature. Water electrolysis test was conducted at 80 °C, showing a cell performance of 1.63 V at 2 A cm^{-2}.

ACKNOWLEDGEMENTS
Financial support for this work is acknowledged from the National Natural Science Foundation of China (grant numbers of 91010002 and 50874008). A Ph.D. scholarship from University of Science and Technology Beijing (USTB) provided the opportunity for JY Xu to visit DTU and complete this work. Support is also acknowledged from the Danish National Research Foundation (the PROCON Center), the Danish Council for Strategic Research (MEDLYS)

References

1. C.J. Winter, *Int. J. Hydrogen Energy,* 34 (2009) S1.
2. L. Barreto, A. Makihira and K. Riahi, *Int. J. Hydrogen Energy*, 28 (2003) 267.
3. F. Marangio, M. Santarelli and M. Calì, *Int. J. Hydrogen Energy,* 34 (2009) 1143.
4. S.A. Grigoriev, V.I. Porembsky and V.N. Fateev, *Int. J. Hydrogen Energy,* 31 (2006) 171.
5. P. Millet, D. Dragoe, S. Grigoriev, V. Fateev and C. Etievant, *Int. J. Hydrogen Energy,* 34 (2009) 4974.
6. S. Siracusano, V. Baglio, C. D'Urso, V. Antonucci and A.S. Aricò, *Electrochim. Acta,* 54 (2009) 6292.
7. A.V. Nikiforov, A.L. Tomás García, I.M. Petrushina, E. Christensen and N.J. Bjerrum, *Int. J. Hydrogen Energy,* 36 (2011) 5797.
8. L.R. Ma, S. Sui and Y.C. Zhai, *J. Power Sources,* 177 (2008) 470.
9. J.Y. Xu, G.Y. Liu, J.L. Li and X.D. Wang, *Electrochim. Acta,* 59 (2012) 105.
10. A.T. Marshall and R.G. Haverkamp, *Electrochim. Acta,* 55 (2010) 1978.
11. X. Wu and K. Scott, *Int. J. Hydrogen Energy,* 36 (2011) 5806.
12. A. Marshall, B. Børresen, G. Hagen, M. Tsypkin and R. Tunold, *Electrochim. Acta,* 51 (2006) 3161.
13. J.B. Cheng, H.M. Zhang, H.P. Ma, H.X. Zhong and Y. Zou, *Int. J. Hydrogen Energy,* 34 (2009) 6609.
14. A.T. Marshall, S. Sunde, M. Tsypkin and R. Tunold, *Int. J. Hydrogen Energy,* 32 (2007) 2320.
15. Z.G. Ye, H.M. Meng, D. Chen, H.Y. Yu, Z.S. Huan, X.D. Wang and D.B. Sun, *Solid State Sci,* 10 (2008) 346.
16. J. Aromaa and O. Forsén, *Electrochim. Acta,* 51 (2006) 6104.
17. F. Ye, J.L. Li, X.D. Wang, T.T. Wang, S.M. Li, H.J. Wei, Q.F. Li and E. Christensen, *Int. J. Hydrogen Energy,* 35 (2010) 8049.
18. Y.N. Zhang, H.M. Zhang, Y.M. Ma, J.B. Cheng, H.X. Zhong, S.D. Song and H.P. Ma, *J. Power Sources,* 195 (2010) 142.
19. W.L. Yao, J. Yang, J.L. Wang and Y. Nuli, *Electrochem. Commun.,* 9 (2007) 1029.
20. C.B. Xu, L.R. Ma, J.L. Li, W. Zhao and Z.X. Gan, *Int. J. Hydrogen Energy,* 37 (2012) 2985.
21. F.D. Kong, S. Zhang, G.P. Yin, Z.B. Wang, C.V. Du, G.Y. Chen and N. Zhang, *Int. J. Hydrogen Energy,* 37 (2012) 59.
22. Y.J. Zhang, C. Wang, N.F. Wan, Z.X. Liu and Z.Q. Mao, *Electrochem. Commun.,* 9 (2007) 667.
23. H.N. Su, B.J. Bladergroen, V. Linkov, S. Pasupathi and S. Ji, *Int. J. Hydrogen Energy,* 36 (2011) 15081.
24. J.Y. Xu, R.Y. Miao, T.T. Zhao, J. Wu and X.D. Wang, *Electrochem. Commun.,* 13 (2011) 437.
25. X. Wu and K. Scott, *Int. J. Hydrogen Energy,* 35 (2010) 12029.
26. H.N. Su, B.J. Bladergroen, S. Pasupathi, V. Linkov and S. Ji, *Int. J. Electrochem. Sci.,* 7 (2012) 4223.
27. T.T. Wang, C.S. Lin, F. Ye, Y. Fang, J.L. Li and X.D. Wang, E *Electrochem. Commun.,* 10 (2008) 1261.
28. M. Srinivasarao, D. Bhattacharyya, R. Rengaswamy and S. Narasimhan, *Int. J. Hydrogen Energy,* 35 (2010) 6356.
29. G.B. Chen, H.M. Zhang, J.B. Cheng, Y.W. Ma and H.X. Zhong, *Electrochem. Commun.,* 10 (2008) 1373.
30. A.D. Li, M. Han, S.H. Chan and N. Nguyen, *Electrochim. Acta,* 55 (2010) 2706.
31. A. Therdthianwong, P. Saenwiset and S. Therdthianwong, *Fuel,* 91 (2012) 192.
32. J.S. Zhao, X.M. He, L. Wang, J.H. Tian, C.R. Wan and C.Y. Jiang, *Int. J. Hydrogen Energy,* 32 (2007) 380.

33. D. You, Y. Lee, H. Cho, J. Kim, C. Pak, G. Lee, K. Park and J. Park, *Int. J. Hydrogen Energy*, 36 (2011) 5096.
34. L.L. Sun, R. Ran and Z.P. Shao, *Int. J. Hydrogen Energy,* 35 (2010) 2921.
35. T. Gan, Q.Z. Jiang, H.J. Zhang, W.L. Wang, X.Z. Liao and Z.F. Ma, *J. Power Sources*,196 (2011) 1899.
36. H.J. Cho, H. Jang, S. Lim, E, Cho, T. Lim, I. Oh, H. Kim and J. Jang, *Int. J. Hydrogen Energy,* 36 (2011) 12465.
37. S. Yim, Y. Sohn, S. Park, Y. Yoon, G. Park, T. Yang and C. Kim, *Electrochim. Acta*, 56 (2011) 9064.
38. J. Xie, K.L. More, T.A. Zawodzinski and W.H. Smith, *J. Electrochem. Soc.*, 151 (2004) A1841.
39. R. Berenguer, C. Quijada and E. Morallón, *Electrochim. Acta,* 54 (2009) 5230.
40. S. Ardizzone, G. Fregonara and S. Trasatti, *Electrochim. Acta*, 35 (1990) 263.
41. T.C. Liu, W.G. Pell and B.E. Conway, *Electrochim. Acta*, 42 (1997) 3541.
42. B.V. Tilak, C.P. Chen and S.K. Rangarajan, *J. Electroanal. Chem.*, 324 (1992) 405.
43. L.A. da Silva, V.A. Alves, M.A.P. da Silva, S. Trasatti and J.F.C. Boodts, *Electrochim. Acta*, 42 (1997), 271.
44. A. Marshall, B. Børresen, G. Hagen, M. Tsypkin and R. Tunold, *Mater. Chem. Phys.*, 94 (2005) 226-32.
45. E. Rasten, G. Hagen and R. Tunold, *Electrochim. Acta,* 48 (2003) 3945.
46. J. C. Cruz, V. Baglio, S. Siracusano, V. Antonucci, A. S. Aricò, R. Ornelas, L. Ortiz-Frade, G. Osorio-Monreal, S. M. Durón-Torres and L. G. Arriaga, *Int. J. Electrochem. Sci.*, 6 (2011) 6607.
47. E. Tsuji, A. Imanishi, K. Fukui and Y. Nakato, *Electrochim. Acta,* 56 (2011) 2009.
48. J.M. Hu, J.Q. Zhang and C.N. Cao, *Int. J. Hydrogen Energy,* 29 (2004) 791.
49. J.B. Cheng, H.M. Zhang, G.B. Chen and Y.N. Zhang, *Electrochim. Acta*, 54 (2009) 6250.
50. X. Wu, K. Scott and V. Puthiyapura, *Int. J. Hydrogen Energy,* 37 (2012) 13243.
51. J.C. Cruz, A.R. Hernández, M. Guerra-Balcazar, A.U. Chávez-Ramirez, J. Ledesma-García and L.G. Arriaga, *Int. J. Electrochem. Sci.,* 7 (2012) 7866.
52. S. Siracusano, V. Baglio, M.A. Navarra, S. Panero, V. Antonucci and A.S. Aricò, *Int. J. Electrochem. Sci.*, 7 (2012) 1532.